Asociación Argentina
de Mecánica Computacional

Mecánica Computacional Vol XXXII, págs. 1027-1045 (artículo completo)
Carlos G. García Garino, Aníbal E. Mirasso, Mario A. Storti, Miguel E. Tornello (Eds.)
Mendoza, Argentina, 19-22 Noviembre 2013

AN EXPERIMENTAL AND KINETIC MODELING STUDY OF BIODIESEL COMBUSTION IN LAMINAR COUNTERFLOW PREMIXED FLAMES

Dario Alviso[a,b], Juan C. Rolon[a], Philippe Scouflaire[b] and Nasser Darabiha[b]

[a]*Laboratorio de Mecánica y Energía , Facultad de Ingeniería, Universidad Nacional de Asunción,
Campus Universitario, San Lorenzo 2160, Paraguay, Email: dalviso@ing.una.py,
http://www.ing.una.py*

[b]*Ecole Centrale Paris, CNRS UPR 288, Laboratoire d'Energétique, Moléculaire et Macroscopique,
Combustion (EM2C), Grande Voie des Vignes, 92290 Chatenay-Malabry, France,
http://www.em2c.ecp.fr*

Keywords: Biodiesel, Counterflow, Premixed Flames, Emission Spectroscopy, OH PLIF, Kinetic Modeling.

Abstract. Biodiesel is a mixture of long chain fatty acid methyl esters used mainly in compression ignition engines. In order to improve engine performance, an understanding of its fundamental properties and the combustion pathways is required. This study presents new data for biodiesel (rapeseed methyl ester, RME) combustion in a laminar counterflow premixed flame configuration (spray biodiesel/air against methane/air) at atmospheric pressure. The visible and ultraviolet (UV) chemiluminescence of the excited radicals CH* and OH*, as well as Planar Laser-Induced Fluorescence (PLIF) of OH are employed experimentally. A new biodiesel surrogate model was developed by combining two skeletal kinetic schemes. CH* and OH* reactions were added to the model. The counterflow flame is simulated, the typical flame structure is presented and a comparison between experimental and numerical OH radical profiles is realized. CH* and OH* experimental and numerical results comparison is also carried out. The numerical predictions of the CH* and OH* mole fraction are very close to the experimental profiles along the central axis.

1 INTRODUCTION

In the context of reduction of fossil fuel consumption, the use of biodiesel is one of the strategies adopted by several countries around the world. However, changing the fuel in diesel engines induces changes in combustion behavior, which can impact pollutants emission.

Indeed, the use of biodiesel in diesel engines decreases emissions of pollutants such as carbon monoxide, unburned hydrocarbons, and particulate matter (Agarwal, 2007), although a slight increase in emissions of nitrogen oxides is observed in some cases (Zheng et al., 2008). Therefore, a better understanding of the biodiesel combustion is needed.

Biodiesel is a complex mixture of methyl esters with different chain lengths and degrees of unsaturation. Due to its complex and long chain methyl ester composition, the number of possible reaction pathways in a chemical reaction mechanism increases drastically. Such mechanisms development is challenging, and its simulations extremely time-consuming as it requires enormous computing resources, even for homogeneous reactors systems. In order to avoid these difficulties, simplified synthetic fuels, called "surrogate fuels", with shorter chain lengths are chosen to carry numerical combustion studies.

The surrogate fuels are structurally similar to actual biodiesel methyl esters. The surrogate chain length has been increased continously over the last years and recently unsaturated surrogates were studied.

In this sense, Seshadri et al. (2009) used the directed relation graph (DRG) method of Lu and Law (2005, 2006) to reduce Herbinet et al. (2008) methyl decanoate $C_{11}H_{22}O_2$ (MD) detailed mechanism to a skeletal mechanism consisting of 125 species and 713 elementary reactions. The model has been validated with experiments studying the limits of ignition and extinction of MD in a counterflow diffusion flame.

More recently, Luo et al. (2012) developed a skeletal mechanism with 115 species and 460 reactions for a tri-component biodiesel surrogate, which consists of methyl decanoate, methyl 9-decenoate $C_{11}H_{20}O_2$ (MD9D) and n-heptane C_7H_{16}. Extensive validations were performed against 0-D simulations with the detailed mechanism and experimental data for spatially homogeneous systems, 1-D flames and 3D-turbulent spray combustion.

A convenient way to experimentally study the flame behavior is to analyze space and time resolved emission of excited radicals CH$(A^2\Delta)$ denoted CH^*, and OH$(A^2\Sigma+)$ denoted OH^*. Indeed, these two radicals are naturally present in the combustion zone and permit to determine important macroscopic properties such as flame location, flame speed and heat release rate fluctuations. However, these two radicals can only be considered as tracer because they have no significant influence on combustion reaction mechanisms. For this reason, CH^* and OH^* are generally not taken into account in reduced kinetic schemes, and comparison with experimental data are consequently not done.

Most of biodiesel surrogates chemical schemes validations were realized employing either homogeneous reactors or counterflow gaseous diffusion flames (Seshadri et al., 2009). Spray counterflow diffusion and premixed flames have been studied by Darabiha et al. (1993); Kee et al. (2011); Alviso et al. (2013). In the present work, we study a counterflow of biodiesel/air against methane/air mixture to carry both experiments and simulations. The simultaneous presence of two different fuels in this configuration is an additional requirement so that the chemical scheme should be able to predict both flames. In this work, we developed a new biodiesel surrogate model, by combining Seshadri et al. (2009) and Luo et al. (2012) skeletal kinetic schemes. CH^* and OH^* formation, chemiluminescence and quenching reactions were added. The available literature data were recently summarized by Panoutsos et al. (2009). Most CH^*

and OH^* reactions and rate constants found in literature (Panoutsos et al., 2009; Elsamra et al., 2005; Smith et al., 2002; Leo et al., 2007) are validated with experiments involving light hydrocarbon flames, such as methane. In a previous work (Alviso et al., 2013), we have validated CH^* and OH^* reactions for Seshadri et al. (2009) MD kinetic scheme. In our knowledge, no validation of the data has yet been made for a biodiesel fuel.

Measurements of CH^* and OH^*OH* emissions and OH PLIF profiles have been realized for a biodiesel laminar counterflow spray premixed flame. By comparing experimental and numerical OH profiles, we seek to verify that the current counterflow burner configuration permits to reproduce similar combustion as the one simulated with the developed kinetic scheme. Then, we seek to validate the production and consumption reactions of CH^* and OH^* in the case of biodiesel flames.

2 EXPERIMENTAL SETUP

2.1 Counterflow Burner Device

The experiments were carried out in a counterflow burner (Figure 1A). The setup used will be described briefly. More information of the burner can be found in Rolon et al. (1991, 1995).

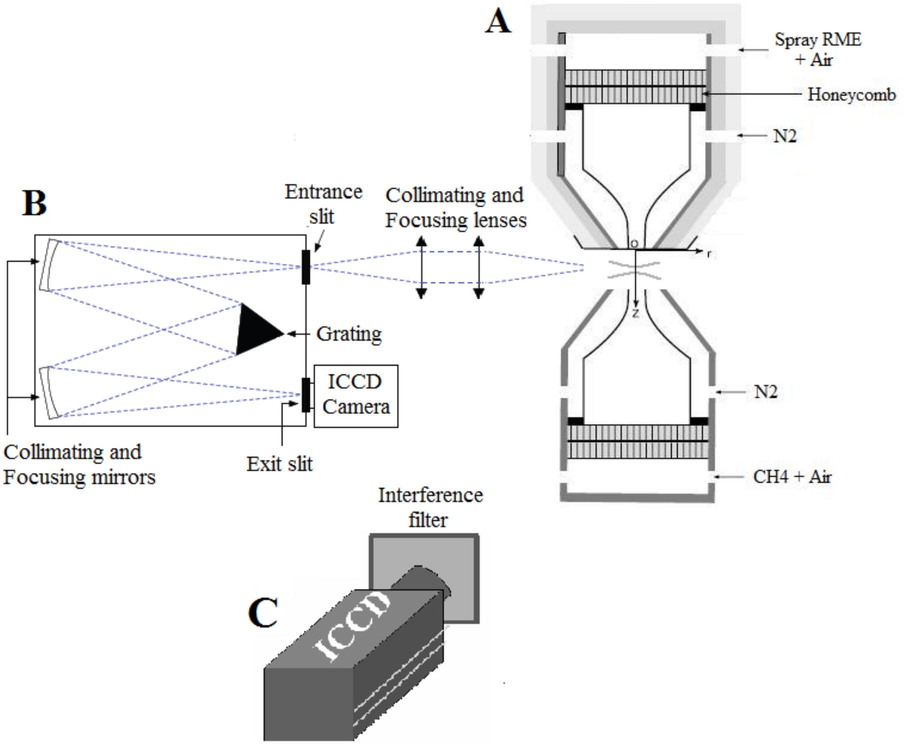

Figure 1: A) Counterflow burner device, B) Emission Spectroscopy setup, C) Visualization setup

The burner consists of two opposed axisymmetric convergent nozzles of 20 mm inner diameter. A premixed gaseous flow of methane and air is injected at ambient temperature through the lower side of the burner, while a spray flow of biodiesel and air is transported at 400 K from the upper side. The biodiesel chosen to carry the experiments is rapeseed-derived biodiesel or rapeseed methyl ester (RME). A laminar flame front appears on each side of the stagnation point. The distance between the two nozzle exits was kept constant to 40 mm. Each nozzle contains two layers of honeycomb to reduce turbulent structures in the plennum chamber of the nozzle. Each nozzle is surrounded by a coaxial nozzle fed by nitrogen in order to protect the flames from ambient perturbations that could disturb the measurements.

The liquid fuel atomizer is the one used in Rolon et al. (1991). The advantage of this system is that the size distribution of the spray is particularly narrow (Durox et al., 1999). The inconvenience is that we were restricted to work with small air flowrates and with very lean biodiesel flames.

The methane flame equivalence ratio is $\phi = 0.62$. The methane/air flow velocity at the injector face is 50.1 cms^{-1} and the mass flow rate per unit area (mass flux) is $5.9 \cdot 10^{-02}$ $gcm^{-2}s^{-1}$. The injection temperature at the lower burner is 300 K.

The biodiesel flame equivalence ratio is ϕ = 0.28. The biodiesel/air flow velocity at the injector face is 29.5 cms^{-1} and the mass flow rate per unit area (mass flux) is $2.9 \cdot 10^{-02}$ $gcm^{-2}s^{-1}$. The biodiesel and air mass flow rates at the upper burner are 0.0069 and 0.307 Kg/h, respectively. The injection temperature at the upper burner is 400 K.

An electrically heated pipe is used to maintain the spray flow heated between the atomizer and the burner. The upper burner is also heated electrically. The surrounding nitrogen is also heated at the same temperature, in order to have a uniform temperature in the upper burner. The whole line and the upper burner are kept at 400 K.

A premixed methane/air flame front is formed at few milimeters from the lower injector exit. The hot burnt gases from the methane/air combustion are located between the flame front and the stagnation plane, and ensure additional heating on the biodiesel/air flame.

All gaseous mass flow rates are controlled by the mass flow meters with an accuracy of $\pm 1.5\%$ and a repeatability of $\pm 0.5\%$ of the full scale. The biodiesel liquid mass flow was measured with an accuracy of $\pm 10\%$. The overall uncertainty of velocities, methane and biodiesel flames equivalence ratios can therefore be estimated at $\pm 2.5\%$, $\pm 1.5\%$ and $\pm 12\%$, respectively.

2.2 Liquid Chromatography / Mass Spectrometry

Biodiesel fuel composition was analyzed with Liquid Chromatography and Mass Spectrometry (LC-MS) technique. The objective of this measurement is to obtain the chemical composition of studied biodiesel fuel. This information is needed to estimate the equivalence ratio of the biodiesel flame, and also it will be used as input to carry the simulations.

The estimation of rapeseed-derived biodiesel concentration and mole fraction is presented in Table 1. In comparison to the literature values (Herbinet et al., 2008), it corresponds to the classical composition of biodiesel obtained from this oil. From this Table, rapeseed-derived biodiesel formula is estimated: $C_{18.9}H_{33.3}O_2$. In order to estimate the measurement precision, the analysis was realized several times. The repeatability observed in the measures for each methyl ester was about 98 %.

The chemical structure of each methyl ester is presented in Figure 2. The structures of these components show the considerable structural similarities in these chemical species, each with a methyl ester attached to a large hydrocarbon chain. Differences are the length of the hydrocarbon chain (15 atoms of carbon for methyl palmitate and 17 atoms of carbon for the other methyl esters) and the number of double bonds in the hydrocarbon chain (no double bond for methyl palmitate and methyl stearate, one double bond for methyl oleate, two for methyl linoleate and three for methyl linolenate).

Rapeseed biodiesel composition		
Methyl ester	CC (ppm)	Mole fraction
Palmitate	417	4.73
Stearate	157	1.78
Oleate	5660	64.21
Linoleate	1866	21.16
Linolenate	715	8.11

Table 1: Composition of rapeseed-derived biodiesel.

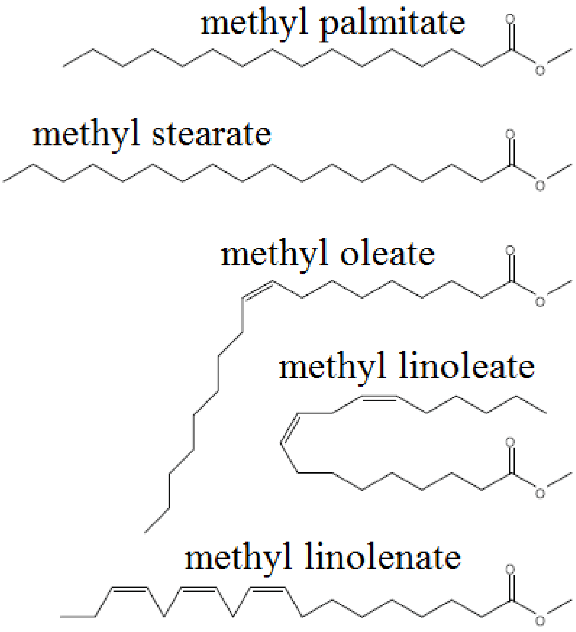

Figure 2: Structures of the main components in rapeseed-derived biodiesel

2.3 Emission Spectroscopy

The visible and UV chemiluminescence of the excited radicals CH^* and OH^* were measured by Optical Emission Spectroscopy (OES). The objective of these measurements is to determine the relative mole fractions of CH^* and OH^* emissions of biodiesel flames with respect to those of methane flame. Thus, emission spectra were not quantitatively calibrated.

Two 500 mm focal length UV lenses were used to focus the light emitted by the flame into the entrance slit of a spectrometer (Acton Research, Model SpectraPro 2750). The grating used had 1200 gratings/mm and the focal length of the spheric mirrors was 750 mm (Figure 1B). The emission spectrum along the burner axis was recorded by a 1024×256 pixels Intensified CCD camera (Roper Scientific, Inc.). A substraction of the ambient background and CO_2 was done.

As the biodiesel flame is very lean, the emission is very low, then a compensation on the slit opening was made, always taking care of having a reasonable spectral resolution. So, for CH^* and OH^*, a slit width of respectively 750 μm and 500 μm were chosen, giving respectively a spectral resolution of 0.3 and 0.27 nm. The exposure time was kept constant to 100 ms. The CH^* population was obtained by making an integration between 420 and 440 nm wavelength, while the OH^* population was acquired between 300 and 320 nm wavelength. However, only the band head of each spectrum was taken into account: the band heads at 431 and 308 nm for CH^* and OH^* radicals, respectively, with a bandwidth of 1 nm each.

For the CH^* and OH^* mole fractions in both flames, an average over 50 images was made. The uncertainty of the measurement was estimated from the CH^* and OH^* maximum mole fractions in the 50 images, in comparison to the average values. For the methane flame it was $\pm 20\%$ and for biodiesel flames it was $\pm 25\%$.

2.4 Visualization

Images of CH^* and OH^* emission have been recorded using a 512×512 pixels ICCD camera (Princeton Instruments) equipped with UV-lens (Nikkor 105 mm focal length) (see Figure 1C).

Narrow-band interference filters were interposed along the optical path for capturing the CH^* and OH^* emission. The filter used for CH^* has 60% transmission and a $10 - nm$ wide bandpass centered around 430 nm. The OH^* filter is centered at 313 nm, $10 - nm$ bandpass and 68% transmission in the maximum.

As these results are complementary to the spectroscopy measurements, the exposure time was fixed to 100 ms and an average over 50 images was made.

Figure 3A presents a typical biodiesel flame front obtained from CH^* visualization. This figure shows that the flame front is slightly convex. The line of sight creates an integrated signal along its trajectory and increases the measured mole fraction. As the flame front is axisymmetrical, Abel inversion (a digital tomography method) is used to eliminate the effects of the integration and get the trace of the flame front in the symmetry plane of the burner as done in Leo et al. (2007); Herding et al. (1998) and Alviso et al. (2013) (Figure 3B, Figure 4). It should be noted that the Abel inversion has shifted slightly the location of the maximum CH^* emission intensity.

The resolution of the CCD camera and the depth of field (about the flame length) limit the accuracy of the vertical positioning along the flame axis to ± 0.2 mm. Then, due to the slight flames oscillation, the flame position was estimated with an accuracy of ± 0.5 mm.

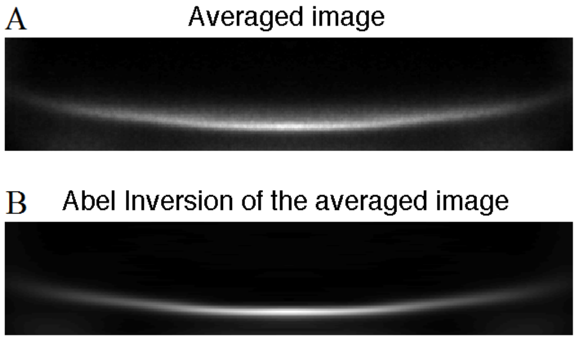

Figure 3: Averaged (A) and Abel inverted (B) image of CH^* emission from biodiesel Flame

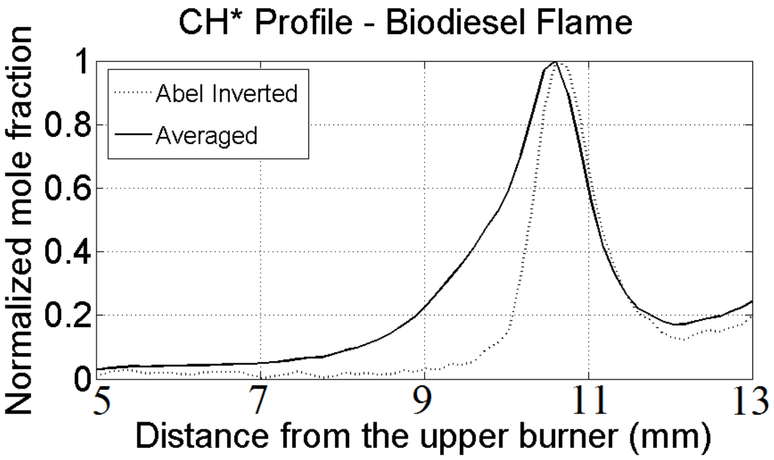

Figure 4: Axial CH^* emission profiles of the averaged and Abel inverted data normalized with the peak values, from biodiesel Flame

2.5 OH PLIF

Figure 5 presents the experimental setup used to realize OH PLIF measurements. The laser sheet dimension was about $30 \times \ 0.5\ mm^2$, and it was transported directly to the flames axis and was positioned in the flame zone.

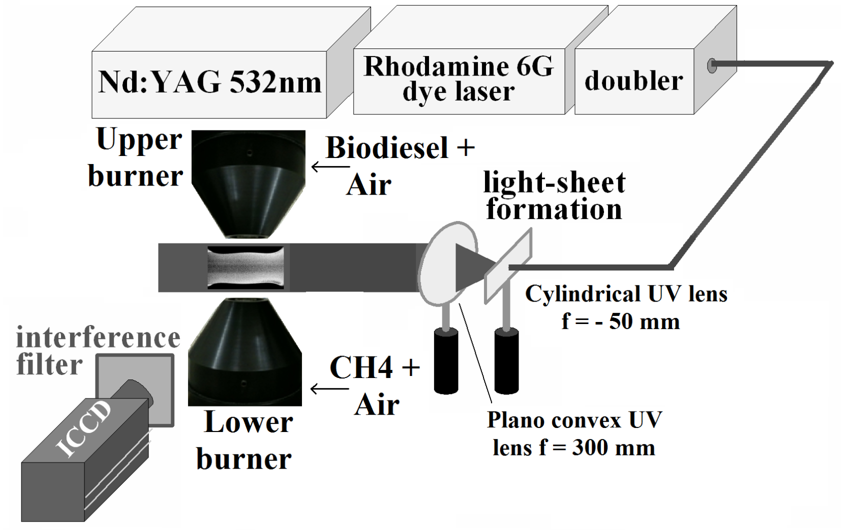

Figure 5: OH PLIF on a counterflow flame setup

The OH radical is excited with a dye laser CONTINUUM $(Rhodamine\ 590)$ pumped by a Nd: YAG laser CONTINUUM doubled $(800\ mJ\ @\ 532\ nm)$. The $Q_1(6)$ OH transition of the Q”=0, Q’=1 band of the $(A^2\Sigma, X^2\Pi)$ system was excited at $283.043\ nm$ with an energy of about $18\ mJ$.

The fluorescence images were collected on the same camera used for the visualization (512×512 pixels ICCD). In this case, the camera gate was kept constant to $20\ ns$. This allows the CCD to drastically reduce the chemiluminescence signals. Furthermore, the same filter used for the OH* visualization was chosen to collect the OH fluorescence signal.

Measurements have been performed in linear regime of fluorescence, for this reason, an estimation of the laser sheet energy was carried out by directing the laser beam to a quartz cell, filled with dodecane, and then visualizing the fluorescence signal with the same ICCD camera. The images were then divided by the recorded laser intensity profiles to compensate for the laser profile fluctuations.

The OH profiles were corrected with the laser sheet energy profile on a single shot basis. An average over 100 OH PLIF images was done, taking into account the slight flames oscillation. As the LIF images were not corrected for quenching, the thermal distribution among energy levels, and saturation effects, the color scale in the resulting images represents pure fluorescence intensity, and does not directly correspond to OH mole fraction. Nevertheless, it was shown that quenching effects on the OH PLIF signals is constant along a counterflow flame (Daguse et al., 1996). For this reason, it may be considered that the OH LIF signals in our experiments are within a calibration constant linearly proportional to the OH mole fraction.

The spatial resolution obtained by the optical arrangements was $120\ \mu m$. Considering the flames central axis and in order to determine the OH profiles from the images, the intensity values are summed up over each horizontal line (100 pixels or 12 mm), and the results will be represented as a function of the axial position.

3 KINETIC MODELING

As it can be seen in Section 2.2, biodiesel is a complex mixture of methyl esters with different chain lengths and degrees of unsaturation. In order to avoid these difficulties, simplified synthetic fuels, called "surrogate fuels", with shorter chain lengths are chosen to carry numerical combustion studies.

In this sense, Seshadri et al. (2009) used the directed relation graph (DRG) method of Lu and Law (2005, 2006) to reduce Herbinet et al. (2008) methyl decanoate $C_{11}H_{22}O_2$ (MD) detailed mechanism to a skeletal mechanism consisting of 125 species and 713 elementary reactions. The chemical structure of methyl decanoate is presented in Figure 6A.

More recently, Luo et al. (2012) developed a skeletal mechanism with 115 species and 460 reactions for a tri-component biodiesel surrogate, which consists of methyl decanoate, methyl 9-decenoate $C_{11}H_{20}O_2$ (MD9D) and n-heptane C_7H_{16} (chemical structures presented in Figure 6).

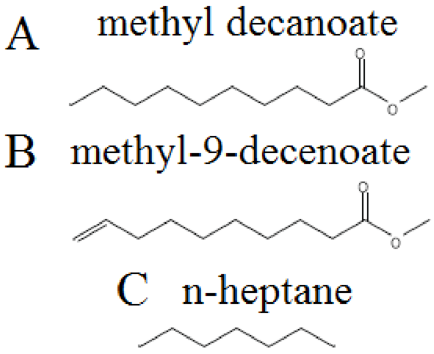

Figure 6: Structures of biodiesel surrogates

Methyl-9-decenoate was chosen because the double bond is at the same position as the one in methyl oleate and at the same location as the first double bond in methyl linoleate and in methyl linolenate (Figure 2).

In this work, the simultaneous presence of two different fuels (biodiesel and methane) is an additional requirement so that the chemical scheme should be able to predict both flames.

Therefore, we have compared Seshadri et al. (2009) and Luo et al. (2012) skeletal kinetic schemes for methane/air combustion and flame speed by performing freely-propagating premixed 1-D flames. The corresponding results are compared to that obtained with a methane kinetic scheme (GRI 3.0 mechanism (Smith et al., 1998)).

The comparison showed that Seshadri et al. (2009) skeletal kinetic scheme does a better job than that of Luo et al. (2012) in reproducing the methane/air combustion and flame speed.

However, Luo et al. (2012) skeletal mechanism includes methyl 9-decenoate, a biodiesel surrogate with one double bond. And as rapeseed-derived biodiesel studied in this work is mainly composed of unsaturated methyl esters (Table 1), $i.e$ methyl esters with one or more double bonds, in this work we combined Seshadri et al. (2009) and Luo et al. (2012) skeletal kinetic schemes.

Therefore, the kinetic model proposed here was designed from the original oxidation framework of methyl decanoate proposed by Seshadri et al. (2009). This chemical scheme was used as a template, and then additional species found in Luo et al. (2012) kinetic scheme and the corresponding reactions were added. Thus, the combined scheme predicts correctly the methane/air combustion and flame speed and also it allows to carry simulations of a unsaturated methyl ester: methyl 9-decenoate. The developed kinetic model consists of 185 species and 911 reactions.

Furthermore, methyl palmitate and stearate (without double bonds) will be represented by MD. And methyl oleate, linoleate and linolenate (with one or more double bonds) will be represented by MD9D. And as the studied rapeseed-derived biodiesel formula is $C_{18.9}H_{33.3}O_2$ (Section 2.2), and the developed model consists of species MD $(C_{11}H_{22}O_2)$ and MD9D $(C_{11}H_{20}O_2)$, in order to keep constant the number of carbon atoms, a factor 18.9/11 was taken into account.

4 NUMERICAL SIMULATION

In a previous work (Alviso et al., 2013), we have employed a surrogate fuel (methyl decanoate) to carry both experiments and simulations under the same configuration. It was shown that the preheated two-phase flow of MD fuel and air completely vaporize before reaching the flame front, and consequently studied spray MD flames can be considered as entirely gaseous.

Therefore in this work, an axisymmetric gaseous biodiesel premixed flame is considered, opposed to a premixed methane flame.

4.1 Governing equations

We consider an axisymmetric counterflow configuration shown in Figure 7. A methane-air mixture is injected from the right side whereas gaseous biodiesel fuel and air are injected from the left side. We model our system using similarity approach by searching for similar solutions of gaseous flow equations in the vicinity of the central axis (Darabiha et al., 1993). These similar solutions have the form: gas density $\rho_g = \rho_g(z)$, gas radial velocity $u_g = r\,U_g(z)$, gas axial velocity $v_g = v_g(z)$, gas temperature $T_g = T_g(z)$ and species mass fractions $Y_k = Y_k(z)$, $k = 1, ...N_{sp}$ (N_{sp} is the number of species).

By assuming a pressure gradient in the radial direction so that $-\frac{1}{r}\frac{\partial p}{\partial r} = J$ is constant along the z axis, the gaseous phase are described by the following balance equations (Darabiha et al., 1993):

$$2\rho_g U_g + \frac{\partial \rho_g v_g}{\partial z} = 0, \tag{1}$$

$$\rho_g U_g^2 + \rho_g v_g \frac{\partial U_g}{\partial z} = \frac{\partial}{\partial z}\left(\mu_g \frac{\partial U_g}{\partial z}\right) + J, \tag{2}$$

$$\rho_g v_g c_{p_g} \frac{\partial T_g}{\partial z} = \frac{\partial}{\partial z}\left(\lambda_g \frac{\partial T_g}{\partial z}\right) - \sum_{k=1}^{K} h_k W_k \Omega_k - \left(\sum_{k=1}^{K} \rho_g Y_k V_{kz} c_{p_{gk}}\right)\frac{\partial T_g}{\partial z}, \tag{3}$$

$$\rho_g v_g \frac{\partial Y_k}{\partial z} = -\frac{\partial}{\partial z}\left(\rho_g Y_k V_{kz}\right) + W_k \Omega_k, \qquad k = 1, ...N_{sp} \tag{4}$$

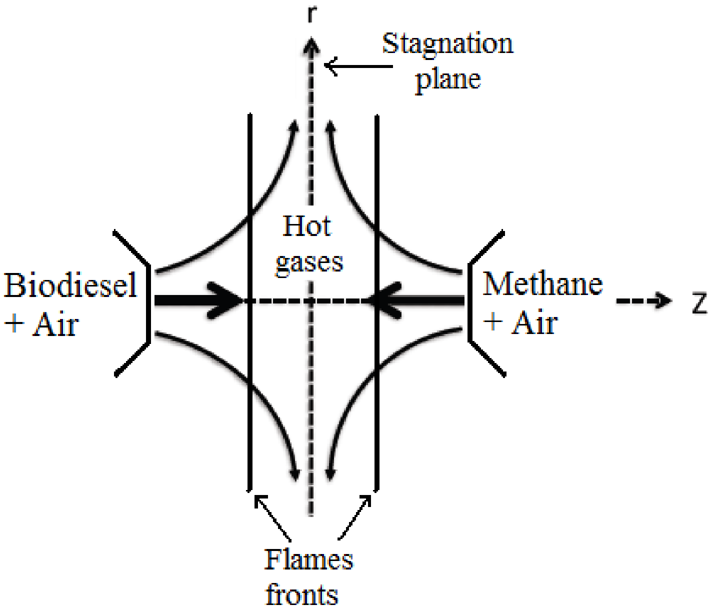

Figure 7: Counterflow premixed flames configuration

In these equations μ_g is the gaseous mixture viscosity. $c_{p_{gk}}$ and c_{p_g} are the heat capacity at local constant pressure of species k and of the mixture respectively. h_k, W_k, Ω_k are the specific enthalpy, the molar weight and the molar chemical production rate of the k^{th} species respectively, and V_{kz} is the diffusion velocity of the k^{th} species in the axial direction.

The above system of equations is completed by the ideal gas equation and by specifying the equation $\frac{\partial J}{\partial z} = 0$.

4.2 Numerical conditions

The boundary conditions of the system are given in Table 2.

	$left\,(z = -20)$	$right\,(z = 20)$
Gas temperature	$T_g = T_g^{left}$	$T_g = T_g^{right}$
Species mass fractions	$Y_k = Y_k^{left}$	$Y_k = Y_k^{right}$
Gas axial velocity	$v_g = v_g^{left}$	$v_g = v_g^{right}$
Gas radial velocity	$u_g = 0$	$u_g = 0$

Table 2: Boundary conditions

The set of equations for the gaseous phase is then replaced by a fully coupled set of discrete relations. The solution of this system is then based on a global adaptive nonlinear method using Newton iterations (see Darabiha et al. (1988); Giovangigli and Smooke (1987)). The grid is adapted to first and second order derivatives of all variables and the smallest grid size is 5 μm.

The kinetic modeling for biodiesel oxidation in the counterflow flame was performed using the REGATH-1D-COUNTERFLOW code of the REGATH package with detailed thermochemical and transport properties developed at EM2C laboratory. The inputs to each simulation include a chemical kinetic reaction mechanism, a dataset of thermochemical properties and a dataset of transport properties.

4.3 CH* and OH* Chemical Reactions

Chemical reactions describing the production, quenching and chemiluminescence of CH* and OH* were added to the developed biodiesel surrogate mechanism. Also species C and C_2 were introduced since they both appear in the CH* production reactions.

As expected, due to the low concentration of the excited species, no significant difference in the results was found with the addition of these elementary reactions. The thermochemical data for CH* and OH* were added as well. The transport coefficients for the excited species were the same as those of the ground state species.

The literature data for different kinetics of formation, quenching and chemiluminescence of CH* and OH* in flames were recently summarized by Panoutsos et al. (2009), where the authors have given 6 submechanisms that account for the formation and destruction of the species CH* and OH*. We have employed the different submechanisms to evaluate the results against our experimental data and the ones with the best agreement were selected. This point will be detailed in Section 5.3.

5 RESULTS AND DISCUSSION

5.1 Typical Flame Structure

Figure 8 presents a typical flame structure. The boundary conditions correspond to those given in Section 2.1. In these figures $z = -20$ corresponds to the upper burner edge and $z = 20$ to the lower burner edge.

In Figure 8 (top) is presented fuels (Methyl decanoate (MD), methyl 9-decenoate (MD9D) and methane (CH_4)) and CH^* species profiles. The premixed methane/air flame front is located at about $z = 0.0\ mm$. The CH^* profile at this point passes through a maximum ($6.23 \cdot 10^{-13}$ mole fraction) and its width at half maximum is $0.2\ mm$. The biodiesel flame front is located at $z = -8.5\ mm$. The maximum CH^* is $1.22 \cdot 10^{-13}$ mole fraction and its width at half maximum is $0.5\ mm$.

The stagnation point (axial velocity $v = 0$) is located at $z = -8.0\ mm$. The equivalence ratio of the biodiesel/air flame is 0.28 and the corresponding flame speed is too small (about 5 $cm\, s^{-1}$), that is why the biodiesel flame front is very close to the stagnation point. The ratio between the X species mole fraction at the biodiesel flame front to the X species mole fraction at the methane flame front will be called R_X. The value of R_{CH^*} is 0.19.

Methyl decanoate (MD) and methyl 9-decenoate (MD9D) species profiles remain constant until $z = -11\ mm$, then decreases rapidly at about $z = -8.7\ mm$, before reaching the biodiesel/air flame front (given by the CH^* peak position). Methane (CH_4) mole fraction remains constant until 18.0 mm from the right injector ($z = 2.0\ mm$), then decreases rapidly at about $z = 0.2$ mm, before reaching the methane/air flame front (given also by the CH^* peak position).

At the biodiesel flame side, methyl decanoate and methyl 9-decenoate fuels decompose to lighter species, but methane is not formed in large quantities ($1.18 \cdot 10^{-05}$ mole fraction).

In Figure 8 (bottom) is presented O_2 and H_2O species and temperature profiles. Concerning O_2 species profile, at the methane flame side the mole fraction remains constant until 18.0 mm from the right injector ($z = 2.0\ mm$), then decreases very sharply at about $z = 0.2$ mm, in a similar way as methane mole fraction presented in Figure 8 (top). At the biodiesel flame side, O_2 mole fraction remains constant until 9.0 mm from the left injector ($z = -11\ mm$), then decreases in a not very sharp way due to the decomposition of MD and MD9D fuels in lighter species. In the zone between flame fronts, as biodiesel and methane flames are both lean ($\phi =$

0.28 and 0.62, respectively), there are O_2 left. The O_2 mole fraction after biodiesel flame is higher than that 'after' methane flame, therefore there is O_2 species diffusion in this zone.

The numerical premixed methane/air flame front is located at about $z = 0.0\ mm$. At this point, the gas temperature increases very rapidly from 300 K to 1600 K within 1 mm. The temperature variation at the biodiesel side is essentially due to heat diffusion across the stagnation point. The heat released by the biodiesel flame front has small influence at this region.

The H_2O mole fraction follows the same type of variation as the gas temperature profile.

5.2 Experimental and Numerical Profiles of OH Radical

Figure 9 gives a comparison between experimental and numerical profiles of the OH radical obtained by PLIF for the biodiesel/air flame.

As the OH measurements are only qualitative, the experimental profiles were normalized by the maximum values of this radical, corresponding to the methane/air flame.

The position of the increase in the OH mole fraction due to the biodiesel and methane flames are very well predicted by the simulation. Furthermore, the relative OH mole fraction of the biodiesel/air flame compared to that of methane/air flame (R_{OH}) is well predicted by the simulation. Moreover, in the hot zone between flame fronts, OH is underestimated by the simulation. This may also be due to the experimental poorer spatial resolution.

5.3 Experimental and Numerical Profiles of CH^* and OH^* Radicals

Figure 10 gives a comparison between experimental and numerical mole fraction profiles of CH^* (top) and OH^* (bottom) radicals for biodiesel/air flame.

As the measurements do not give absolute values, in order to make comparisons with the numerical results, the experimental profiles of CH^* and OH^* were normalized by their maximum values, corresponding to the methane/air flame front. Also, it was chosen to present the curves of OH^* in logarithmic scale, because the maximum peak mole fraction of biodiesel/air flames is considerably lower than that of the methane/air flame (R_{OH^*} is too small).

The ratios R_{CH^*} and R_{OH^*} will be used to analyze the CH* and OH* submechanisms. The experimental values of $R^{exp}_{CH^*}$ and $R^{exp}_{OH^*}$ are 0.1091 and 0.0076, respectively.

Among the 6 studied submechanisms describing the production, quenching and chemiluminescence of CH^* and OH* (Panoutsos et al., 2009), the one suggested by Smith et al. (2002), who proposed a rate constant for OH* formation by measuring absolute concentrations of OH^* in a flat premixed low-pressure methane-air flame, gives the best prediction of R_{CH^*} and R_{OH^*} ratios, which are equal to 0.1987 and 0.0062, respectively, to be compared to the experimental values $R^{exp}_{CH^*} = 0.1091$ and $R^{exp}_{OH^*} = 0.0076$.

We should note that all six submechanisms have the same elementary reactions and corresponding rate constants for quenching and chemiluminescence of CH* and OH*. For OH* they are $OH^* + M \rightleftharpoons OH + M$ and $OH^* \Rightarrow OH + h\nu$, respectively, where h is Planck constant and ν is the wavelength of chemiluminescent emission. The main difference between the six submechanisms concerns the CH^* and OH^* formation reactions. Smith et al. (2002) formation reactions are presented in Table 3.

As we can see in Figure 10, the numerical predictions of CH^* and OH^* mole fractions are very similar to the experimental profiles along the axis. The positions of the biodiesel and methane flame peaks match almost perfectly. The experimental profiles are slightly thicker than the simulated ones, however this can be explained by the poorer spatial resolution in the experiments.

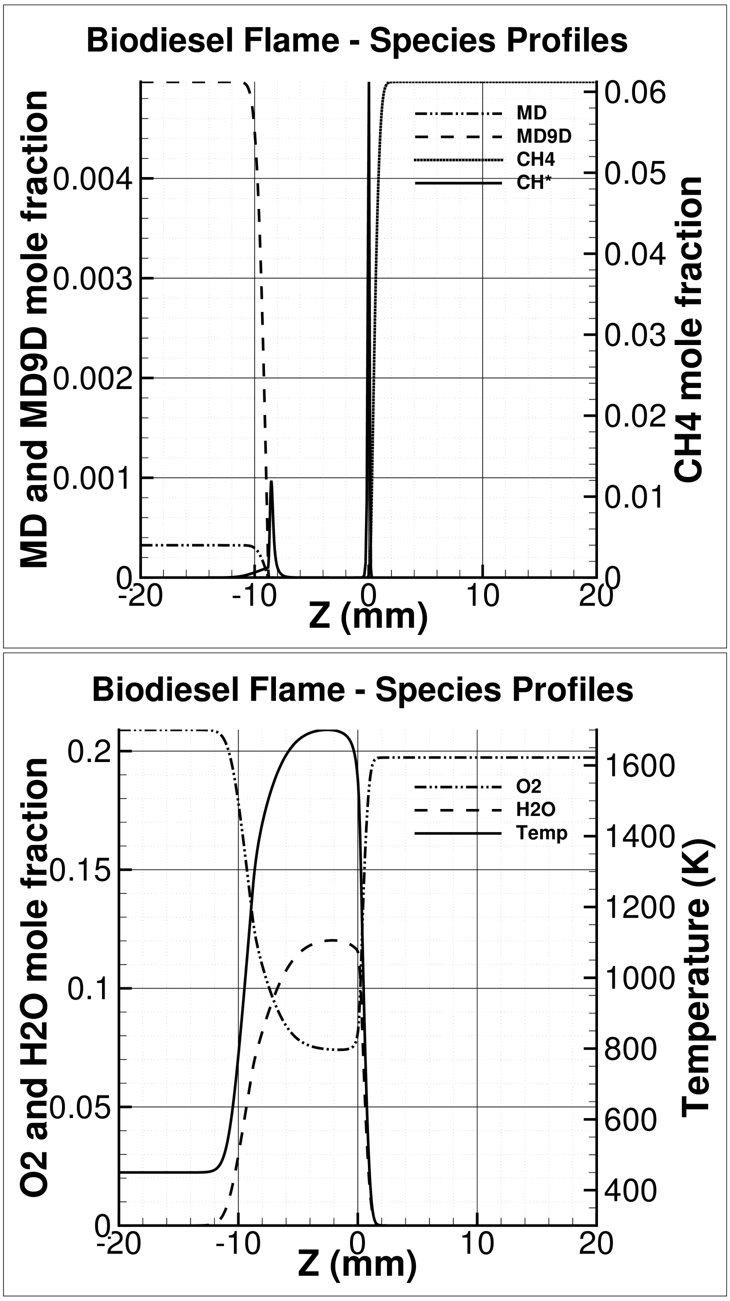

Figure 8: Methyl decanoate (MD), Methyl 9-decenoate (MD9D), methane (CH_4) and CH^* species profiles of biodiesel flame (top), O_2 and H_2O species and temperature profiles of biodiesel flame (bottom)

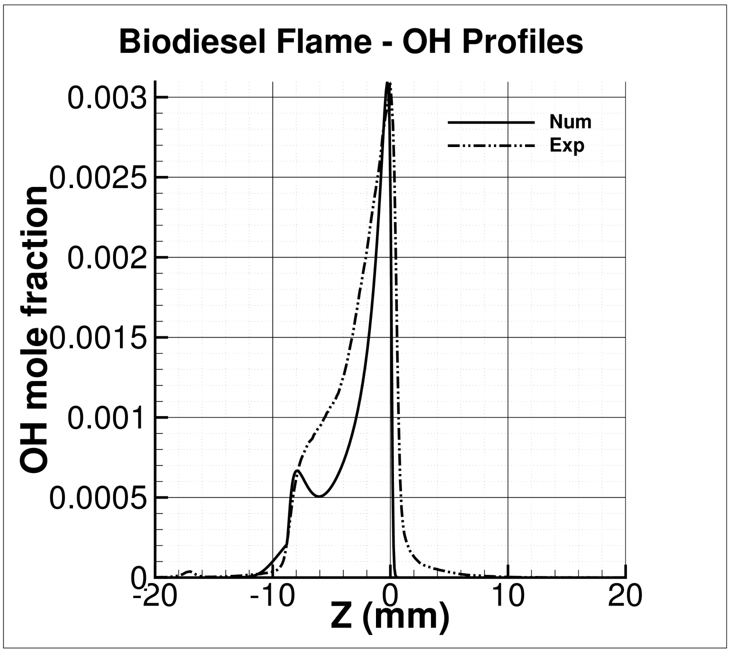

Figure 9: Comparison between the experimental and numerical OH radical profiles of biodiesel flame

		Smith et al. (2002)		
#	Reactions	A	n	E
R1	$C_2H + O \Leftrightarrow CO + CH^*$	6.2×10^{12}	0	0
R2	$C + H + M \Leftrightarrow CH^* + M$	3.63×10^{13}	0	0
R3	$CH + O_2 \Leftrightarrow CO + OH^*$	1.8×10^{11}	0	0
R4	$O + H + M \Leftrightarrow OH^* + M$	3.63×10^{13}	0	0

Table 3: CH* and OH* formation reactions

Reaction rate coefficients given in the form $k = AT^n exp(-E/RT)$. Units are mol cm cal s

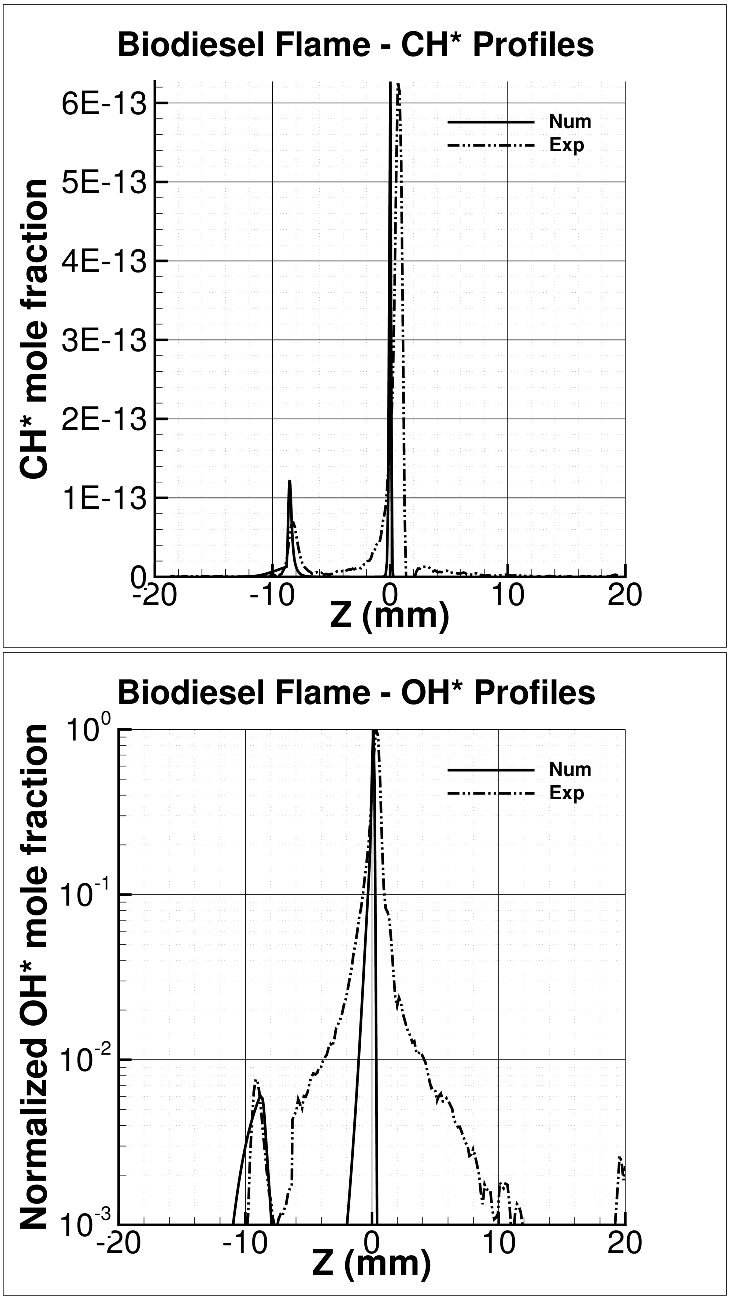

Figure 10: Comparison between experimental and numerical profiles of CH^* (up) and OH^* (bottom) radicals for biodiesel flame

Considering the very small mole fractions of the measured species ($1.23{\cdot}10^{-13}$ and $1.40 \cdot 10^{-13}$ for biodiesel CH^{*} and OH^{*} mole fraction, respectively) and the uncertainties in the chemical excitation modeling, the predictions quality with the skeletal biodiesel surrogate kinetic model is very good.

The agreement is good when comparing $R_{CH^{*}}$ and $R^{exp}_{CH^{*}}$. The production of CH^{*} is inherently sensitive to the predicted mole fraction of species C_2H, C and H through reactions (R1) and (R2) (see Table 3).

The agreement is notable when comparing $R_{OH^{*}}$ and $R^{exp}_{OH^{*}}$. The production of OH^{*} is inherently sensitive to the predicted mole fraction of species CH, O and H through reactions (R3) and (R4) (see Table 3).

6 CONCLUSION

This work presents an experimental and numerical study of rapeseed-derived biodiesel combustion.

The first step of this work was to design a setup that permits to study the behavior of such flames. For that, a counterflow configuration was chosen with, on the lower part of the burner, stabilization of a lean premixed flame of methane and air, and on the upper part, stabilization of spray biodiesel and air flame. Measurements of CH* and OH* emission profiles have been realized, as well as OH species profiles.

A convenient way to experimentally study the flame behavior is to analyze space and time resolved emission of CH* and OH*. In biodiesel surrogate reduced kinetic schemes, CH* and OH* are not taken into account, and comparison with experimental data are consequently not done. For this reason, CH* and OH* reactions were added to the reduced biodiesel surrogate kinetic scheme.

In this work, a new biodiesel surrogate model was developed by combining Seshadri et al. (2009) and Luo et al. (2012) skeletal kinetic schemes. The kinetic model proposed here was designed from the original oxidation framework of methyl decanoate proposed by Seshadri et al. (2009). This chemical scheme was used as a template, and then additional species found in Luo et al. (2012) kinetic scheme and the corresponding reactions were added. Thus, the combined scheme predicts correctly the methane/air combustion and flame speed and also it allows to carry simulations of a unsaturated methyl ester: methyl 9-decenoate. The developed kinetic model consists of 185 species and 911 reactions.

By comparing experimental and numerical OH profiles, we have verified that the counterflow burner permits to reproduce similar combustion as the one simulated with the developed reduced mechanism.

Concerning the CH^{*} and OH^{*} experimental and numerical results comparison, the predictions quality with the skeletal biodiesel kinetic model is very good. In particular, the relative value of the local maximum CH^{*} and OH^{*} concentrations at the biodiesel flame front with respect to that of methane flame front ($R_{CH^{*}}$ and $R_{OH^{*}}$) are very well predicted.

7 ACKNOWLEDGMENT

This research was supported by Itaipu Binacional (Paraguay) and EM2C laboratory (France). The PhD is being conducted in co-supervision at Laboratorio de Mecánica y Energía - Facultad de Ingeniería, Universidad Nacional de Asunción and Laboratoire EM2C - UPR CNRS 288, Ecole Centrale Paris. Rapeseed-derived biodiesel fuel was analyzed at the University of Paris Sud (France), using Liquid Chromatography-Mass Spectrometry technique.

REFERENCES

Agarwal A. Biofuels (alcohols and biodiesel) applications as fuels for internal combustion engines. *Progress in Energy and Combustion Science*, 33:233 – 271, 2007.

Alviso D., Scouflaire P., Lacoste D., Darabiha N., and Rolon J.C. Experimental and numerical characterization of the methyl decanoate combustion in laminar counterflow spray premixed flames. *Proceedings of the ASME 2013 Turbo Expo 2013, San Antonio, USA*, 2013.

Daguse T., Croonenbroek T., Rolon J., Darabiha N., and Soufiani A. Study of radiative effects on laminar counterflow h2/o2n2 diffusion flames. *Combustion and Flame*, 106(3):271 – 287, 1996. ISSN 0010-2180. doi:10.1016/0010-2180(95)00251-0.

Darabiha N., Candel S., Giovangigli V., and Smooke M. Extinction of strained premixed propane-air flames with complex chemistry. *Combustion Science and Technology*, 60:267 – 285, 1988.

Darabiha N., Lacas F., Rolon J., and Candel S. Laminar counterflow spray diffusion flames: A comparison between experimental results and complex chemistry calculations. *Combustion and Flame*, 95(3):261 – 275, 1993. ISSN 0010-2180. doi:10.1016/0010-2180(93)90131-L.

Durox D., Ducruix S., and Lacas F. Flow seeding with an air nebulizer. *Experiments in Fluids*, 27:408 – 413, 1999.

Elsamra R.M.I., Vranckx S., , and Carl S.A. Ch($a^2\delta$) formation in hydrocarbon combustion the temperature dependence of the rate constant of the reaction $c_2h + o_2 \rightarrow ch(a^2\delta) + co_2$. *The Journal of Physical Chemistry*, 109:10287–10293, 2005.

Giovangigli V. and Smooke M.D. Extinction of strained premixed laminar flames with complex chemistry. *Combustion Science and Technology*, 53:23 – 49, 1987.

Herbinet O., Pitz W.J., and Westbrook C.K. Detailed chemical kinetic oxidation mechanism for a biodiesel surrogate. *Combustion and Flame*, 154(3):507 – 528, 2008. ISSN 0010-2180. doi:10.1016/j.combustflame.2008.03.003.

Herding G., Snyder R., Rolon C., , and Candel S. Investigation of cryogenic propellant flames using computerized tomography of oh emission images. *Journal of Propulsion and Power*, 13:146 – 151, 1998.

Kee R.J., Yamashita K., Zhu H.Y., and Dean A.M. The effects of liquid-fuel thermophysical properties, carrier-gas composition, and pressure, on strained opposed flow non-premixed flames. *Combustion and Flames*, 158(6):1129–1139, 2011.

Leo M.D., Saveliev A., Kennedy L.A., and Zelepouga S.A. Oh and ch luminescence in opposed flow methane oxy-flames. *Combustion and Flame*, 149(4):435 – 447, 2007. ISSN 0010-2180. doi:10.1016/j.combustflame.2007.01.008.

Lu T. and Law C.K. A directed relation graph method for mechanism reduction. *Proceedings of the Combustion Institute*, 30(1):1333 – 1341, 2005. ISSN 1540-7489. doi:10.1016/j.proci.2004.08.145.

Lu T. and Law C.K. Linear time reduction of large kinetic mechanisms with directed relation graph n-heptane and iso-octane. *Combustion and Flame*, 144(12):24 – 36, 2006. ISSN 0010-2180. doi:10.1016/j.combustflame.2005.02.015.

Luo Z., Plomer M., Lu T., Som S., Longman D.E., Sarathy S., and Pitz W.J. A reduced mechanism for biodiesel surrogates for compression ignition engine applications. *Fuel*, 99(0):143 – 153, 2012. ISSN 0016-2361. doi:http://dx.doi.org/10.1016/j.fuel.2012.04.028.

Panoutsos C., Hardalupas Y., and Taylor A. Numerical evaluation of equivalence ratio measurement using oh and ch chemiluminescence in premixed and non-premixed methane-air flames. *Combustion and Flame*, 156(2):273 – 291, 2009. ISSN 0010-2180. doi:

10.1016/j.combustflame.2008.11.008.

Rolon J., Aguerre F., , and Candel S. Experiments on the interaction between a vortex and a strained diffusion flame. *Combustion and Flames*, 100:422 – 429, 1995.

Rolon J.C., Veynante D., Martin J.P., and Durst F. Counter jet stagnation flows. *Experiments in Fluids*, 11:313 – 324, 1991.

Seshadri K., Lu T., Herbinet O., Humer S., Niemann U., Pitz W.J., Seiser R., and Law C.K. Experimental and kinetic modeling study of extinction and ignition of methyl decanoate in laminar non-premixed flows. *Proceedings of the Combustion Institute*, 32(1):1067 – 1074, 2009. ISSN 1540-7489. doi:10.1016/j.proci.2008.06.215.

Smith G.P., Golden D.M., Frenklach M., Moriarty N.W., Eiteneer B., Goldenberg M., Bowman C.T., Hanson R.K., Song S., Jr. W.C.G., Lissianski V.V., and Qin Z. Gri-mech 3.0. 1998.

Smith G.P., Luque J., Park C., Jeffries J.B., and Crosley D.R. Low pressure flame determinations of rate constants for oh(a) and ch(a) chemiluminescence. *Combustion and Flame*, 131(12):59 – 69, 2002. ISSN 0010-2180. doi:10.1016/S0010-2180(02)00399-1.

Zheng M., Mulenga M.C., Reader G.T., Wang M., Ting D.S.K., and Tjong J. Biodiesel engine performance and emissions in low temperature combustion. *Fuel*, 87(6):714 – 722, 2008. ISSN 0016-2361. doi:10.1016/j.fuel.2007.05.039.